CHAPTER II

THEORIES AND PRINCIPLES

The concepts of low-dimensional nanostructures are reviewed in this chapter. The principles of self-assembled growth technique and mechanism consisting of molecular beam epitaxy growth mode, self-assembled growth in Stranski Krastanow mode and droplet epitaxy technique are presented. Then, the theory of motivated application of this work, quantum information processing is explained. Finally, the characteristics of material used in this work, GaAs, $In_{0.5}Ga_{0.5}P$ and InP are presented.

2.1 Basic Concepts of Low-dimensional Nanostructures

Carriers, elementary charges or excitations (excitons), in an unconfined or bulk semiconductor are free to move in every direction. With respect to the degree of freedom of carrier movement, bulk is a three dimensional (3D) structure. When reducing dimension one by one leading to a quantum well (QW) and a quantum wire (QWR) structure, carriers can only move in a plane or two spatial dimensions (2D) and in one direction (1D), respectively. While shirking another dimension trends to a quantum dot (QD) structure which completely confines carrier in all three dimensions (0D). The decreased dimensionality of the free-carrier motion results in the modification of carrier's density of states (D.O.S.) which is used to analyze the electronic structure. The D.O.S. gives a measure of the maximum number of carriers that can occupy in an energy range. Depending on the dimensionality of the structure, figure 2.1 shows that the D.O.S. changes from a continue distribution in bulk to a discrete one, delta-function-like, in a QD. A QD is sometime so-called *an artificial atom* because the discrete energy levels form quantum effects are similar to that of an atom.

In each low-dimensional nanostructure, carriers are spatially confined in one or more directions. The length scale in confining direction has to be the order of the de Broglie wavelength (carrier wavelength), $\lambda_{\text{de Broglie}}$ that is a function of a carrier effective mass, m^*, and temperature, T as

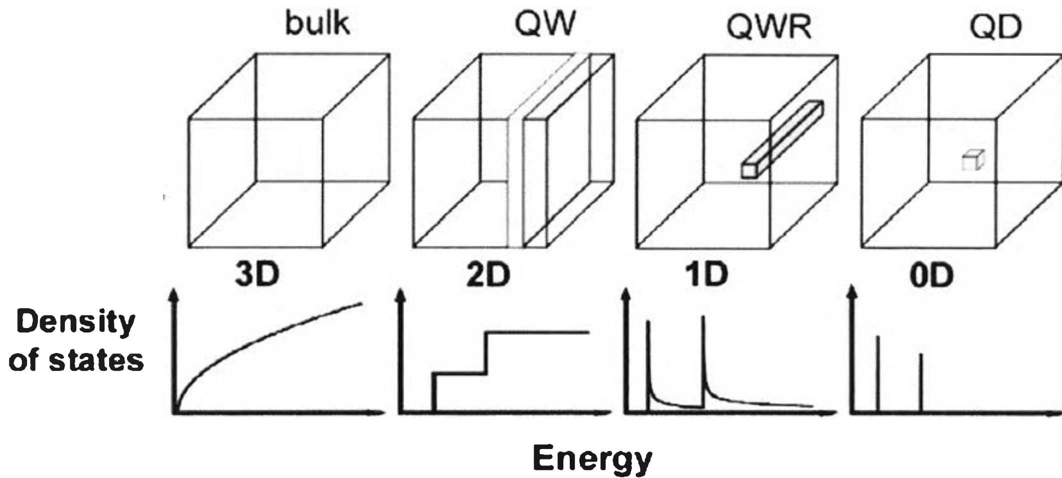

Figure 2.1 Schematic views and graphs of density of states (D.O.S.) in semiconductor structures of decreasing dimensionality: bulk (3D), quantum well (2D), quantum wire (1D), quantum dot (0D).

$$\lambda_{\text{deBroglie}} = \frac{h}{p} = \frac{h}{\sqrt{3m^{*}k_{B}T}} \tag{2.1}$$

where h is Planck's constant (6.626176×10^{-34} JHz^{-1}), p is carrier momentum, and k_{B} is Boltzmann's constant (1.380662×10^{-23} JK^{-1}).

Many attempts have been made to calculate the energy levels of low-dimensional nanostructures especially QD through complicated numerical models that include realistic shapes and the effects of strain (Pryor, 1998; Stier et al., 1999; Wang et al., 1999; Yang et al., 2000.). But to gain a qualitative understanding, energy levels and electronic states of bulk semiconductors and all low-dimensional nanostructures are often discussed in terms of the effective mass approximation (Chuang, 1995; Bimberg et al., 1999). The main assumption of the effective-mass approximation is that the envelope wave function does not significantly vary in the unit cell with a length scale of subnanometers (Wolfe et al., 1989; Bastard and Brum, 1986; Weisbuch and Vinter, 1991). Assuming parabolic band dispersion, band-edge electron states of bulk semiconductors and all low-dimensional nanostructures can be determined from the standing-wave solutions by the Schrödinger equation as

$$\left[-\frac{\hbar^2}{2m^*}\nabla^2 + V(\mathbf{r})\right]F(\mathbf{r}) = E\,F(\mathbf{r}) \tag{2.2}$$

where m^* is the carrier effective mass, $\hbar$ is the reduced Planck's constant ($h/2\pi$, 1.0545887×10^{-34} Js) , $\mathbf{r} = (x,y,z)$ is the carrier position vector, $V(\mathbf{r})$ is the confinement potential; $F(\mathbf{r})$ is the envelope wave function, and E is the carrier energy.

From equation (2.2), by assuming the confinement potential barrier with infinite height, the carrier energy (E) in case of bulk, QW, QWR and QD can be written as

$$E_{\text{bulk}} = E(\mathbf{k}) = \frac{\hbar^2 k^2}{2m^*} \tag{2.3}$$

$$E_{\text{QW}} = E(\mathbf{k}) = \frac{\hbar^2 k_{//}{}^2}{2m^*} + E_{n,z} \tag{2.4}$$

$$E_{\text{QWR}} = E(\mathbf{k}) = \frac{\hbar^2 k_{\perp}{}^2}{2m^*} + E_{m,y} + E_{n,z} \tag{2.5}$$

$$E_{\text{QD}} = E_{l,x} + E_{m,y} + E_{n,z} \tag{2.6}$$

where $\mathbf{k} = (k_x, k_y, k_z)$ is the wave vector of carriers, $k^2 = k_x^2 + k_y^2 + k_z^2$, $k_{//}{}^2 = k_x^2 + k_y^2$, and $k_{\perp}{}^2 = k_x^2$. The energies $E_{l,x}$, $E_{m,y}$, and $E_{n,z}$, which are functions of the potential $V(\mathbf{r})$ depend on the quantum numbers l, m, and n. These energies can be determined by solving equation (2.2) using either analytical method (with some approximations) or numerical methods.

The D.O.S. per unit volume ($D(E)$) which is the number of states between the energy E and $E + dE$, of each structure is written as (Sugawara, 1999)

$$D_{\text{bulk}}(E) = \frac{1}{2\pi^2}\left(\frac{2m^*}{\hbar^2}\right)^{3/2} E^{1/2} \tag{2.7}$$

$$D_{\text{QW}}(E) = \frac{m^*}{\pi\hbar^2}\sum_n \Theta(E - E_{n,z}) \tag{2.8}$$

$$D_{\mathrm{QWR}}(E)=\frac{N_{wi}}{\pi}\frac{\sqrt{2m^{*}}}{\hbar}\sum_{m,\,n}\frac{1}{\sqrt{E-E_{m,y}-E_{n,z}}} \qquad (2.9)$$

$$D_{\mathrm{QD}}(E)=2N_{D}\sum_{l,\,m,\,n}\delta(E-E_{l,x}-E_{m,y}-E_{n,z}) \qquad (2.10)$$

where Θ is the Heaviside's unit step function, N_{wi} is the area density of the QWRs (the number of QWRs divided by the QWR region area in the *y-z* plane), δ is the delta function, and N_D is the volume density of the QD. The D.O.S. in equations (2.7)-(2.10) are schematically shown in figure 2.1 corresponding to their structures.

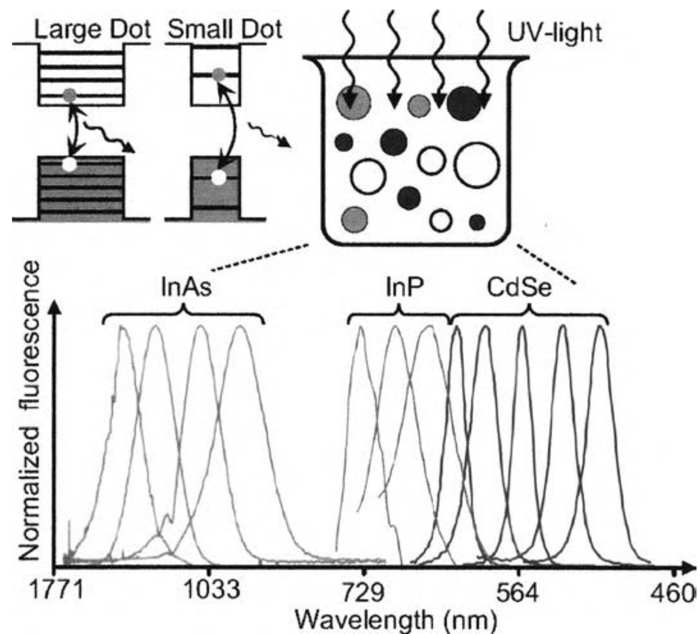

Figure 2.2 Size- and material-dependent emission spectra of several surfactants coated semiconductor nanocrystal QDs (NCQDs) in a variety of sizes. The blue spectral lines are emitted by CdSe NCQDs with diameters of 2.1, 2.4, 3.1, 3.6, and 4.6 nm (from right to left). The green series is emitted by InP NCQDs with diameters of 3.0, 3.5, and 4.6 nm. The red series is emitted by InAs NCQDs with diameters of 2.8, 3.6, 4.6, and 6.0 nm. Within each color the wavelength is fine tuned by controlling the size of the QDs. The inset shows schematically the dependence of the fluorescence energy on the size of the QDs. (Redrawn from Hitchman, 1993)

From equations (2.6) and (2.10), the energy levels and the spacing of discrete electron level of the QDs depend on the potential function, therefore they can be controlled by changing the depth of the potential or the size and shape of the QDs. The example of the energy dependence in form of the emitted wavelength on the QD size is shown in figure 2.2.

2.2 Strain Effect on Low-Dimensional Nanostructures

The self-assembled QDs are obtained by highly lattice mismatched heteroepitaxy, therefore, the understanding of the effects of strain on the material properties is very important. In the case of lattice-matched epitaxy, the deposited material has almost the same lattice constant as that of the substrate material. If the deposited material has a different lattice constant from the substrate, it induces stress and strain to the system because of the Poisson effect. The strain is classified into two types namely compressive and tensile. Figure 2.3 shows the structural aspects of lattice-matched and lattice-mismatched system.

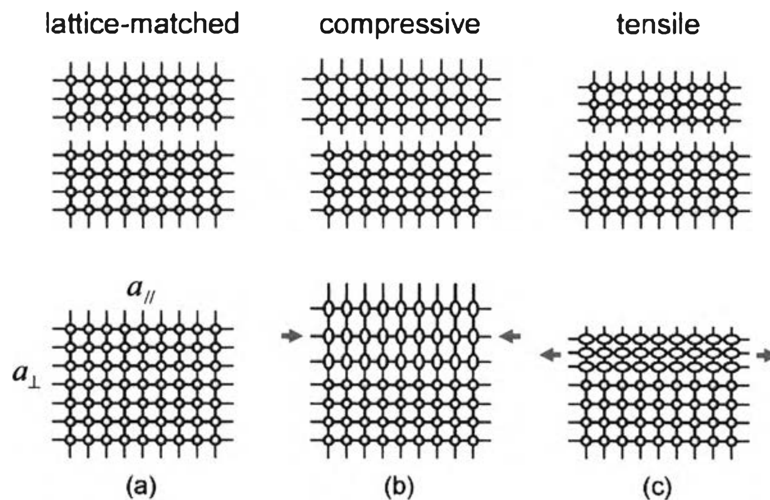

Figure 2.3 Schematic representation of (a) unstrained layer, (b) compressive strained layer, and (c) tensile strained layer. The closed circles represent atoms of the substrate material and the open circles are atoms of the deposited material. In (b) and (c) the lattice constant of the deposited material are different from the epitaxial layer. The arrows in (b) and (c) represent forces (stresses) exerted on the epitaxial layer.

During coherent growth of the layers, the epitaxial atoms match the in-plane lattice constant of the substrate material, as schematically shown in the lower panel of figure 2.3 (b) and (c). This condition induces the biaxial stress and strain in the lateral direction that is associated with the lattice mismatch. These lateral direction stress and strain also change the lattice constant of the deposited material in growth direction which induces the stress and strain in this growth direction continually. If the parallel lattice constant of epitaxial layer is forced to shrink or a compress strain is applied, the perpendicular lattice constant will grow. Conversely, if the parallel lattice constant of epitaxial layer is forced to expand under a tensile strain, the perpendicular lattice constant will shrink. The lattice mismatch or misfit strain (ε) is given by (Bhattacharya, 1997)

$$\frac{\Delta a}{a_s} = \frac{a_e - a_s}{a_e} = -\varepsilon \tag{2.11}$$

where a_e is the lattice constant of the deposited material and a_s is the lattice constant of the substrate. In case of the growth of a strained epitaxial film of thickness d_l with lattice constant a_e on the substrate of thickness d_0 with lattice constant a_s, where $a_e > a_s$, the parallel ($a_{//}$) can be derived by

$$a_{//} = \frac{a_e d_1 - a_s d_0}{d_1 + d_0} \tag{2.12}$$

In general $d_l >> d_0$, therefore

$$a_{//} = a_s = (1-\varepsilon)a_e \tag{2.13}$$

and the perpendicular lattice constant ($a_{\perp}$) is defined as

$$a_{\perp} = (1-\sigma_{ST}\varepsilon)a_e \tag{2.14}$$

where σ_{ST} is a material parameter which is given by

$$\sigma_{ST} = \frac{C_{11}}{2C_{12}} \tag{2.15}$$

where C_{11} and C_{12} are elastic constants of the epitaxial layer.

Assuming that the in-plane coordinate directions are x and y and the growth occurs along z direction coinciding with the (001) crystallographic axis strained growth generates stress upon the x and y directions. The stress components in the x and y directions are equal and force the lattice constants in both of the parallel directions (ε_{xx} and ε_{yy}) to be equal. Therefore, the in-plane strain ($\varepsilon_{//}$) is defined as

$$\varepsilon_{//} = \varepsilon_{xx} = \varepsilon_{yy} = \varepsilon \tag{2.16}$$

During coherent growth of the layers, no compressive strain is generated upon the epitaxial layer in the z direction, but the tensile strain in this direction will be still nonzero. The perpendicular strain ($\varepsilon_{\perp}$) and the strain in growth direction (ε_{zz}) are defined as

$$\varepsilon_{\perp} = \varepsilon_{zz} = -\left[\frac{2\upsilon_{PR}}{(1-\upsilon_{PR})}\right]\varepsilon \tag{2.17}$$

where υ_{PR} is Poisson's ratio which is given by

$$\upsilon_{PR} = \frac{C_{12}}{(C_{11}+C_{12})} \tag{2.18}$$

Therefore

$$\varepsilon_{\perp} = \varepsilon_{zz} = -\frac{2C_{12}}{C_{11}}\varepsilon \tag{2.19}$$

Note that: Poisson's ratio values are close to 1/3 for tetrahedral semiconductors, so these semiconductors have $\varepsilon_{\perp} \approx \varepsilon_{//}$.

The strain energy (E_{st}) per unit area of overlayer of thickness d_1 on a substrate of infinite thickness is given by

$$E_{st} = \varepsilon^2 \left(C_{11} + C_{12} - \frac{2C_{12}^{\ 2}}{C_{11}} \right) d_1 \tag{2.20}$$

The effects of strain on the band structure can be expressed in terms of deformation potentials. The conduction band (CB) is shifted upward for compressive strain and downward for tensile strain. From the deformation potential theory (O'Reilly, 1989), the CB minimum is shifted with respect to average valence band (VB). The heavy-hole (HH) and light-hole (LH) bands, which are initially degenerated, decoupled and shifted in opposite directions as depicted in the figure 2.4. Under biaxial compression, the compression increases the mean band gap and splits the degeneracy of the VB maximum to an anisotropic VB structure. Under biaxial tension, the mean band gap reduces and the VB splitting is reversed.

In the case of a strained quantum well structure, the energy band diagram of the VB can be schematically drawn as shown in the lower part of figure 2.4. The actual number of quantized energy levels of both heavy holes and light holes also depend on the size of the structure and the material parameters.

For the case of self-assembled QD structure, the strain distribution is more complicated due to the three-dimensional nature of this structure. This strain distribution has been widely calculated by several groups (Wang and Zunger, 1999; Bimberg et al., 1999) based on various approaches such as using Green's tensor (Faux and Pearson, 2000). However, the lack of knowledge in exact QD shape, size and composition hinders the accurate prediction of this effect. An example of numerical calculation for a pyramidal QD using finite difference scheme by Bimberg et al. (1999) is given in figure 2.5.

Deformation potential theory is limited to coherent growth of strained layer. An important concept in strained layer epitaxy is that of critical layer thickness. Critical thickness arises because of a competition between strain energy and chemical energy. Below the critical thickness, the minimum energy state of the bilayer system is achieved by strain. Above the critical thickness, the minimum energy state is achieved by formation of dislocations. The critical thickness of the strained layer was first studied by Frank and van der Merwe in thermodynamic equilibrium. This value depends on several parameters, not only on material properties but also on growth conditions. The theoretical and experimental data on this subject can be found in several references (O'Reilly, 1989;

Morkoç et al., 1993; Tsao, 1993; Pimpinelli and Villain, 1998). The critical thickness (h_c) as a function of strain is defined as (Fritz et al., 1985)

$$h_c = \frac{a_s\left(1-\frac{\upsilon_{PR}}{4}\right)\left[\ln\left(\frac{h_c\sqrt{2}}{a_s}\right)+1\right]}{2\sqrt{2}2\pi|\varepsilon|(1+\upsilon_{PR})} \tag{2.20}$$

It is evident that the larger the mismatch, the smaller the critical thickness. The critical thickness can be approximated as $h_c \cong a/2\varepsilon$ which is derived form energy minimization considerations.

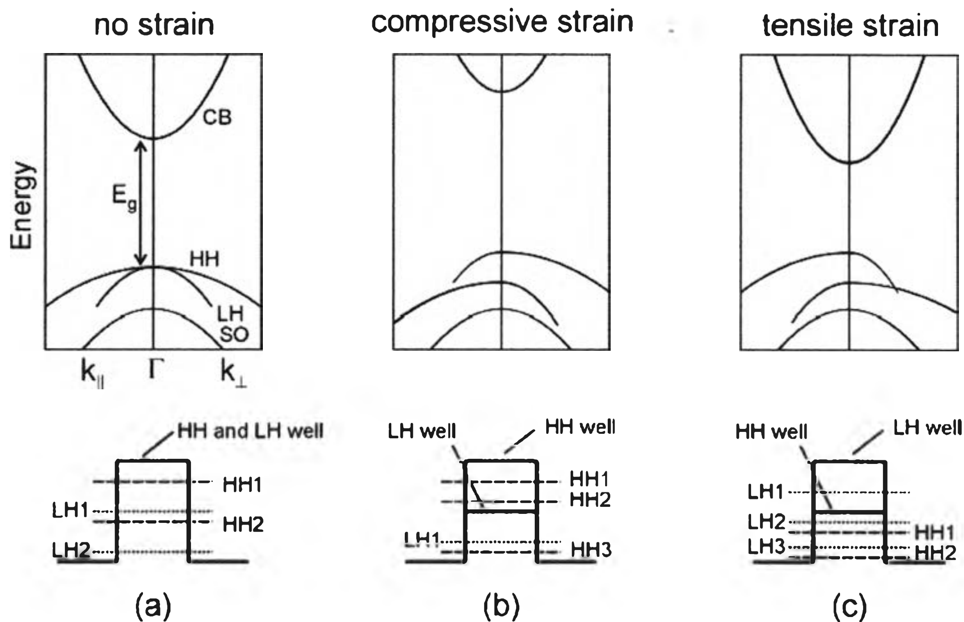

Figure 2.4 (a) A schematic representation of the band structure of an unstrained direct-gap tetrahedral semiconductor. The light-hole (LH) and heavy-hole (HH) bands degenerate at the Brillouin zone center Γ and the spin-split-off (SO) band lies lower in energy. The lowest conduction band (CB) is separated by the band gap energy (E_g) from the valence bands. Note that the $k_{\parallel}$ is perpendicular to the growth and strain direction. (b) Under biaxial compression. (c) Under biaxial tension. The lower panel shows the VB diagram of the quantum well structure in case of (a) unstrained, (b) compressive strained and (c) tensile strain. (Redrawn from O'Reilly, 1989)

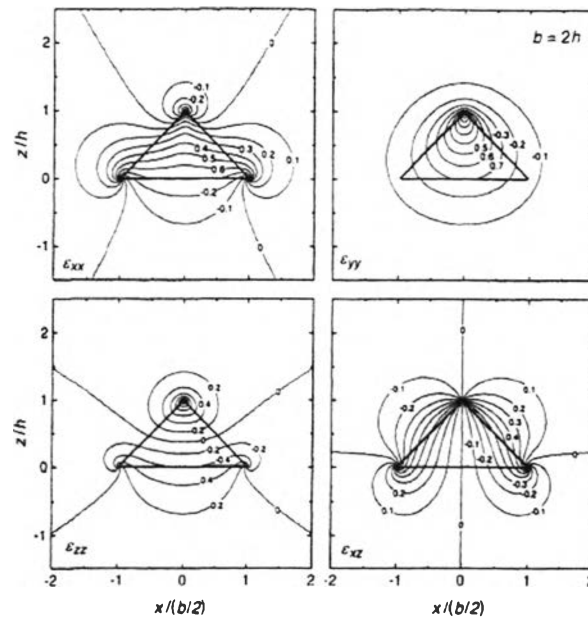

Figure 2.5 Strain distribution for a pyramidal QD with a 45° facet angle in the (xz) plane through the pyramid top. Identical isotropic elastic constants and σ = 1/3 are taken throughout the structure. ε_{xx}, ε_{yy}, ε_{zz}, ε_{xz} are shown; due to symmetry in this plane, ε_{xy}, and ε_{yz} are zero. (Bimberg et al., 1999)

2.3 Growth of Self-Assembled Quantum Dots

QDs investigated in this study are prepared by a molecular beam epitaxy (MBE) system. Without the artificial patterning, self-assembled QDs are coherently trained and their growth is essentially free of defects and impurities. In this work, the Stranski Krastanow growth and the droplet epitaxy technique are utilized to grow self-assembled QDs. To realize a high quality structure, it is necessary to control the spontaneous formation of the QD arrays in the fabrication process including the physical mechanism governing the islands formation, their shape, size, size distribution and the relative arrangement on the surface.

2.3.1 Molecular Beam Epitaxy Growth Modes

The concept of self-assembled QD is based on the lattice mismatch between deposited layer and surface substrate. In this heteroepitaxial growth case, there are three

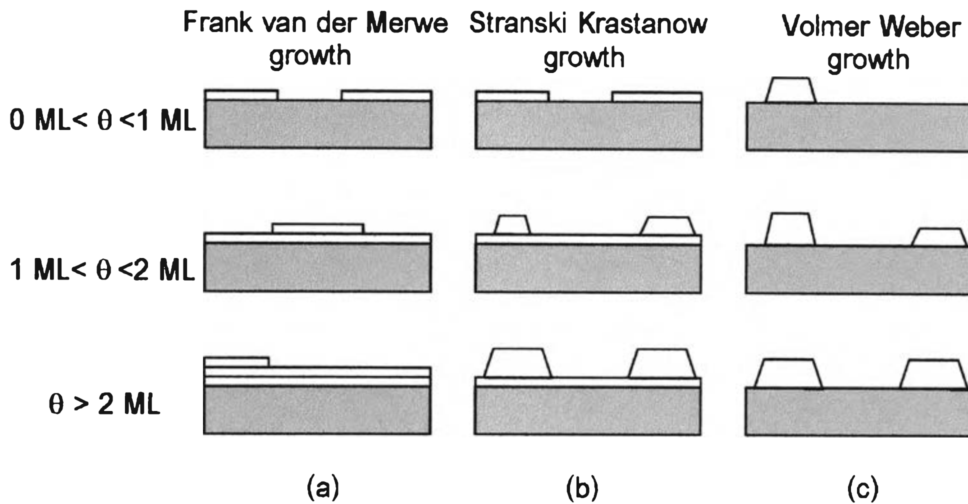

Figure 2.6 Schematic representations of the three crystal growth modes
(a) Layer-by-layer or Frank van der Merwe (FM),
(b) Island or Volmer Weber (VW),
(c) Layer-plus-island or Stranski Krastanow (SK).

possible modes of crystals growth on surface (Michler, 2000; Gilmer and Grabow, 1987): (a) Frank van der Merwe (FM) or layer-by-layer growth, (b) Volmer Weber (VW) or island growth and (c) Stranski Krastanow (SK) or layer-plus-island growth. These modes are illustrated schematically in figure 2.6.

Each growth mode will be adopted in a given system depends on the surface free energy of the substrate/vacuum interface (γ_s) that of the film the epilayer/vacuum interface (γ_e) and epilayer/substrate interface (γ_i). FM growth mode occurs when:

$$\Delta\gamma = \gamma_e + \gamma_i - \gamma_s \leq 0 \tag{2.21}$$

The condition of FM growth mode is rigorously fulfilled only for homoepitaxy (same film material as that of the substrate), where $\gamma_s = \gamma_e$ and $\gamma_i = 0$. If the FM growth mode condition is not fulfilled, $\Delta\gamma > 0$, three-dimensional crystals form immediately on the substrate (VW growth mode). Here, rendering a uniform layer thermodynamically unstable against a break-up into regions where the substrate is covered and those where it is uncovered. For a system of $\Delta\gamma \leq 0$ with a large lattice mismatch between the substrate and the film, initial growth is layer-by-layer but the film is strained. As the film grows in

grows in thickness, it stores increasingly large strain energy. This strained epilayer system can lower its total energy by forming isolated thick islands in which the strain is relaxed by interfacial misfit dislocations, leading to SK growth in these strained systems. SK growth mode occurs when there is a lattice mismatch between the substrate and the epilayer, causing the epilayer to be strained. Growth of dot-like self-assembled islands is a consequence of that.

In case of SK growth mode, the growth proceeds in an intermediate case. After forming a few monolayers in FW growth mode, the islands are formed on top of this "intermediate" layer, which is generally called the wetting layer (WL).

2.3.2 Self-Assembled Growth in Stranski-Krastanow Growth Mode

The illustration of island formation in SK growth mode is shown in figure 2.7. In this growth condition, the first few monolayers of the deposited material form in to 2D platelets which proceed in layer by layer mode until they merge with each other to complete 2D epilayer. During the growth, elastic strain energy, E_{elastic} builds up and increases linearly due to the lattice mismatch and the deposited volume (Seifert et al., 1996):

$$E_{\text{elastic}} = E_{st}\, A = \varepsilon^2 \lambda\, d_l\, A \tag{2.22}$$

where E_{st} is strain energy per unit area from equation (2.20) which has λ represents as the elastic modulus, ε is the lattice mismatch that can determine by equation (2.11), A is the surface area and d_l is the film thickness. Beyond the critical thickness, the layer-by-layer growth is unfavorable, the strain energy outweigh the surface energy the system has to release the strain energy by changing the growth mode from 2D to 3D growth mode, causing the island formation (Slolovitz, 1989).

Although the QDs grown by this technique form into high density arrays and do not need any *ex situ* processing. there are still some disadvantages of this technique. For example, we can not precisely control the locations of the QDs even though many groups have attempted to achieve this goal (Kohmoto et al., 2002; Lee et al., 2000). The control of location is very important for using QDs in nanoelectronic applications.

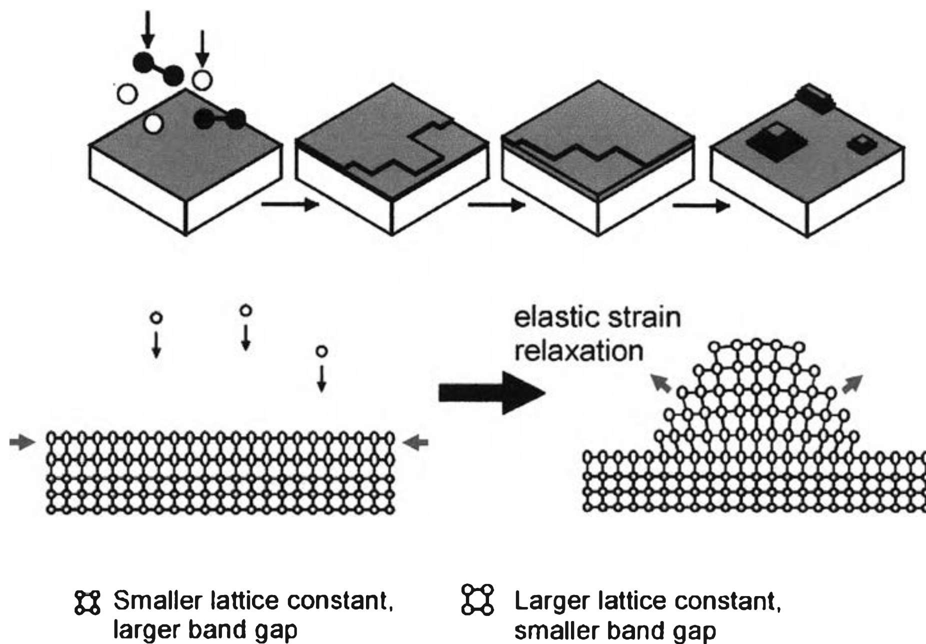

Figure 2.7 Schematic representations of island formation during epitaxial growth of a semiconductor material on top of another one with a smaller lattice constant in Stranski-Krastanov growth mode.

2.3.3 Thermodynamic and Kinetic Theories of Self-Assembled Quantum Dot Formation in Equilibrium System

In general, the theoretical work on self- assembly can be grouped into two classes. First aspect explains the QD formation by using energetic principles and equilibrium thermodynamics (Shchukin et al., 1995; Daruka and Barbasí, 1997). Second, since some properties of QD formation clearly exhibit nonequilibrium features, the dynamic models are invented to explain such a feature (Dobb et al., 1997; Barbasí, 1997; Meixner et al. (2001)). This section will descriptively present the island formation mechanism in both thermodynamic and kinetic approach.

2.3.3.1 Thermodynamically Limited Growth

Thermodynamic theory of 3D coherently strained island growth, was proposed by Shchukin et al. (1995), explains the narrow size distribution of islands by considering the energetic of an array of islands. This model was supported by several groups (e.g.

Spencer and Tersoff, 1997; Wang et al., 2000; Medeiros-Ribeiro et al. 1998). Based on energy minimization, highly strained coherent 3D islands equilibrate into ensembles with equilibrium size. The total energy of a coherently strained 3D QD or island, E_{island}, can be written as a sum of three contributions as

$$E_{island} = E_{elastic} + E_{surf} + E_{edge} \tag{2.23}$$

where $E_{elastic}$ is the elastic strain energy, E_{surf} is the surface energy of the island, and E_{edge} is the island edge energy. Assuming that the island has a pyramidal shape with a squared base size L, the energy per unit volume of the L-dependent terms can be expressed as follows (Bimberg et al., 1999)

$$E(L) = E_0\left[-2\left(\frac{L_0}{L}\right)^2 \ln\left(\frac{e^{1/2}L}{L_0}\right) + \frac{2\alpha}{e^{1/2}}\left(\frac{L_0}{L}\right)\right] \tag{2.24}$$

where α is a control parameter which is a function of surface energy and elastic strain energy of QD structure. The α value can be positive or negative. The E_0 and L_0 are the characteristic energy and the characteristic length of the pyramid, where α=0 respectively. The relationship of island energy per unit volume and base size L are plotted in figure 2.8 for different values of the control parameter α. The analysis from equation (2.21) reveals that:

If $\alpha \leq 1$, the ripening of islands is occurs and is a stable array. The optimum island size (L_{opt}) corresponding to the absolute minimum of energy, where $\min E(L) \equiv E(L_{opt}) < 0$.

If $E(L) \to 0$, the ripening of islands corresponds to $L \to \infty$, therefore the islands do not undergo ripening. Only an array of identical islands with optimum island size is a stable array.

If $1 < \alpha < 2e^{-1/2} \approx 1.2$, there is only a local minimum of the energy corresponding to a metastable array of islands, where $E(L) > 0$.

If $\alpha > 1.2$, the local minimum in the energy $E(L)$ disappears.

For both cases where $\alpha > 1$, there is a thermodynamic tendency towards ripening. This energy minimum corresponds to a single huge cluster, where all deposited material is collected (Shchukin and Bimberg, 1999).

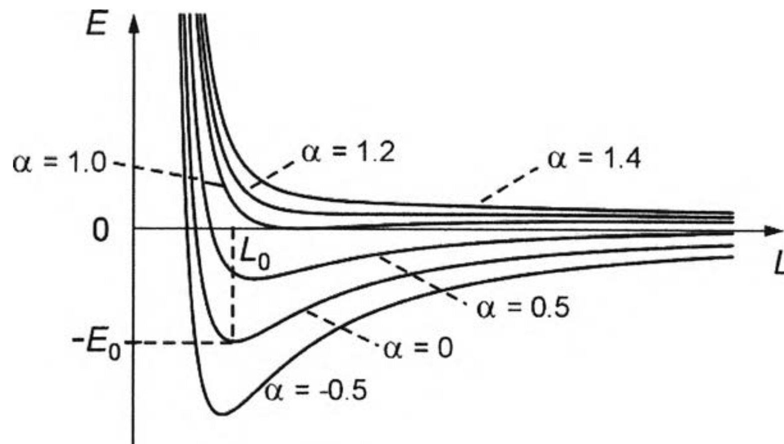

Figure 2.8 Energy of an array of 3D coherently strained islands per one atom versus island size L. The control parameter α depends on the contribution from the surface energy and the edge energy (Bimberg et al., 1999).

The more understanding of equilibrium morphology of the system can be achieved by taking into account the existence of the WL. Owing to mass conservation of QD material between the WL and QD with neglecting desorption and interdiffusion, the thickness of WL and the total volume of all islands are not separately fixed. The energy stored in the WL must take into account to minimize the energy of system. This model was introduced by Daruka and Barabási (1997). The total energy per unit cell (E) of this system is given by

$$E = E_{WL}(Q_1) + Q_2 E_{island}(Q_2) + (Q - Q_1 - Q_2)E_{rip} \tag{2.25}$$

here the energy of the wetting layer is $E_{WL}(Q_1)$, $E_{\text{island}}(Q_2)$ is the energy of 3D pyramids per atom which has a little different form compared to that of the definition in eq. (2.23) E_{rip} is energy of ripened island. Q is the ML-thickness of material that are deposited, Q_1 is the ML-thickness form the wetting layer, Q_2 ia the ML-thickness assembled in 3D coherently strained islands of a given pyramidal shape and volume, and the rest of the material, which is equal to $Q\text{-}Q1\text{-}Q2$ MLs, is assembled in the ripened islands. (Shchukin and Bimberg, 1999; Daruka and Barabási, 1997).

By minimizing the energy in equation (2.25) with respect to Q_1 and Q_2, the equilibrium phase diagram of a lattice-mismatched heteroepitaxial system as a function of

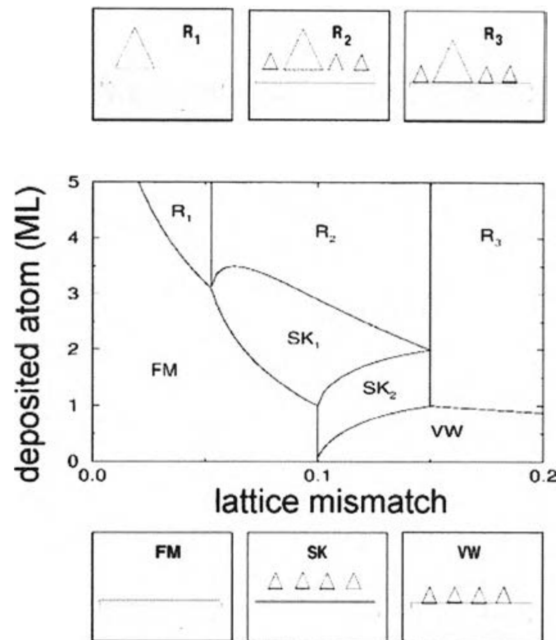

Figure 2.9 Equilibrium phase diagram of lattice-mismatched heteroepitaxial system as a function of the total amount of deposited material and lattice mismatch. The small panels on the top and the bottom illustrate the morphology of the surface in the six growth modes. The small empty triangles indicate the presence of stable islands, while the large shaded ones refer to ripened islands (Daruka and Barabási, 1997).

the lattice mismatch ε and of the total amount of the deposited material Q can be obtained. The calculated phase diagram is shown on figure 2.9 (Daruka and Barabási, 1997; Merz et al., 1999; Barabási et al., 2000).

From the thermodynamic theories developed by Shchukin et al. (1995) and Daruka and Barabàsi (1997), they conclude that the QDs are formed because they are energetically more favorable than 2D growth and ripening. However, the thermodynamic theories can not provide several aspects during the growth of the QDs. For example, the growth of the QDs is generally known to depend on the growth rate, which can not be explained by the equilibrium theory. Moreover, the predicted tendency of the QD size on the growth temperature from this theory can not be explained (Meixner et al., 2001). Finally, the effects of the entropy, which is excluded in this consideration, should be considered in order to explain the QD size and the size distribution.

2.3.3.2 Kinetically Controlled Growth

The kinetic theory of growth is another theory which provides an effective prediction of the QD formation mechanism. The kinetic approach can give an understanding of the island formation and growth as a function of growth parameters such as growth rate, growth temperature and substrate temperature. Several kinetic models of 3D island formation have been proposed (Chen and Washburn, 1996). These models are usually based on time-dependent calculations such as nucleation theory, kinetic Monte Carlo simulation and mean-field theory (Schöll and Bose, 1998; Barabási, 1997; Dobbs et al., 1997). Such models take the microscopic processes on the crystal surface into account such as deposition, diffusion, attachment to the island and detachment from islands. In this section, the kinetically controlled growth of QDs in a qualitative way is described.

The atomic processes are described by the mean-field theory that the deposited atoms arrive at the surface and become adatoms. Then, the number of adatoms increases constantly during the initial growth. The adatoms migrate on the surface and collide with one another and then nucleate into small 2D islands (platelet). Thermal fluctuations can break up these small 2D islands into adatoms again by reducing sizes less than a critical value. During further material deposition, 2D islands become larger due to the attachment of new-coming adatoms. If the 2D island size exceeds the limiting value, the growth of these islands will change from the 2D to 3D growth mode. The adatoms can also attach to or detach from the nucleated 3D islands at the rates determined by the related energy contribution. By solving the mean-field rate equations obtained from the atomic processes described above, the dependence of the 3D island or QD density on the growth parameters such as temperature and growth rate can be accurately predicted (Dobbs et al., 1997). As a function of the growth rate and substrate temperature, the island density appears to be controlled by the 2D island nucleation that the density is an increasing function of the growth rate and a decreasing function of temperature. The island density increases rapidly at the early stage of the deposition and then saturates. Further depositing material does not significantly effect to the island density but leads to the increasing of the island size.

Another kinetic aspect, which can describe the limited size of the QDs, is the self-limiting Growth (Seifert et al., 1996; Chen and Washburn, 1996; Jesson et al., 1998). Figure 2.10 (a) shows a schematic of the local strain energy density in and around a 3D

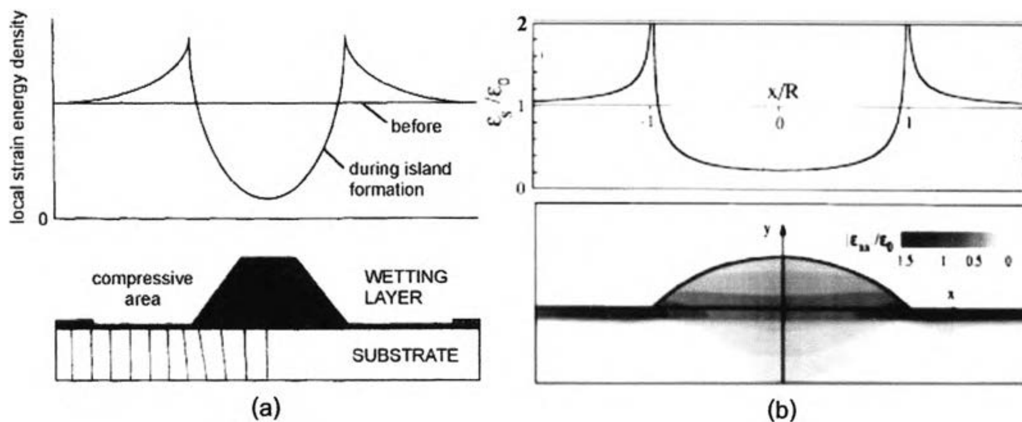

Figure 2.10 (a) Schematic representation of the local strain energy density in and around the QD. The energy barrier for the adatom's diffusion to the QD has a maximum at the edge of the QD (Seifert et al., 1996) and (b) The variation of the surface strain ε_s along the system surface and a contour diagram showing strain ε_{xx} in the island (Chen and Washburn, 1996).

island during the island formation (Seifert et al., 1996). The appearance in this energy density due to the formation of the 3D island affects the surface chemical potential. The minimum of the potential locates at the top of the island where the material partially relaxes, while the maximum is at the island edge, where the high compressive strain exists. The compressive strain at the island edge propagates down to the substrate, increasing an inherent misfit between the substrate and the wetting layer around the island. Therefore, the high potential barrier around the island provides a zone, where the islands do not prefer to nucleate. Since the increase of the potential around the coherent islands depends on the island size, its formation has a self-limiting effect on the growth of the coherent islands. The surface strain approximated by using an analytic solution of a surface tangential strain ε_s along the system surface, the stress field in 2D mound on a strained semi-infinite substrate as a contour plot of absolute value of ε_{xx} and are shown in figure 2.10 (b). Chen and Washburn (1996) also derived the growth rate due to this effect and found that the growth rate decreases while the island size increases.

In additions, Barabási (1997) proposed that for the large islands, the strain energy at the island edge becomes comparable to the bonding energy of the edge atoms, enhancing the detachment of the atoms at the island edge and consequently causing

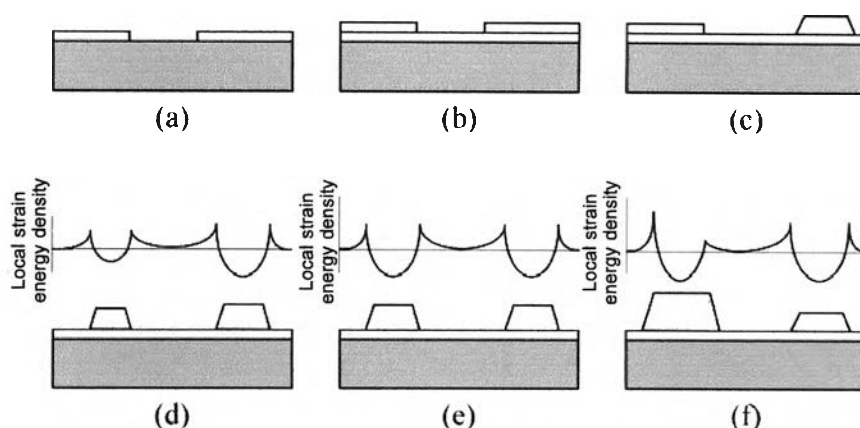

Figure 2.11 Schematic illustration of SK QDs formation process (a) initial stage of wetting layer formation (b) the wetting layer (c) 2D to 3D islands transition, (d) non-uniform 3D islands (e) self-regulation process and (f) misfit dislocation formation.

gradual island dissolution. The two mechanisms lead the size uniformity. Further material deposition cause the growth of the exist islands. As a consequence, the high strain energy occurs at the edge of the larger island. The formation of the misfit dislocation at the island edge is one way to relieve the strain energy of the system; the energy barrier would decrease and enhance the directional migration of adatoms to this island. The strain relief in the island with dislocation decreases the energy barrier and then permits the further growth of the island. The process permits the resumption of the island growth to reach the second critical size. The process of the QDs formation from these kinetic models can summarize as the schematic illustration from (a) to (f) shown in figure 2.11.

2.3.4 Self-Assembled Growth by Droplet Epitaxy Technique

The fabrication of QDs by self-assembling SK growth mode utilizing equilibrium process has already been discusses as a basic knowledge for the growth of QDs. Contrasting to the SK growth mode, the droplet epitaxy technique utilizes nonequilibrium process for fabricating quantum-confined nanostructures. This technique has many unique advantages including (i) the growth can be performed at lower temperature system than the conventional growth (ii) can be used both in lattice-mismatched and in lattice-matched material system (iii) this method can fabricate not only QDs but also QRs and

complex nanostructures and (iv) the liquid nature of the droplet tends to produce dislocation free and coherence nanostructures.

The droplet epitaxy technique includes two basic processes (Mano, 2000; Mano and Koguchi, 2005) as shown in figure 2.12. First, group III elements with a low melting point are applied on the surface under the absence of the group V element supplying, creating liquid metal droplets. The group III metal droplets are formed due to the bonding energy between incoming group III atoms (adatoms) is much higher than that between the surface and the adatoms. After that, the newly formed liquid metal droplets are then converted into semiconductors under the supply of group V flux which is so-called the crystallization. These two processes are correlated to each other and hence determine the final shape of nanostructures. Due to the growth rate at the droplet periphery is more than that inside the droplet, the size and shape formation of resultant nanostructures is based on the initial dimension of the droplets, the atom migration and diffusion process, and the group V flux intensity condition during crystallization. If the group V flux intensity is high enough to diffuse into the droplets and to cooperate at the droplet periphery at the same time, the nanostructures will form to be the QD structure similar to the initial droplet. In the case of group V flux intensity is applied with lower pressure, the nanostructures can form to be the quantum ring (QR) like structure by the migration of group III atoms to higher growth rate region.

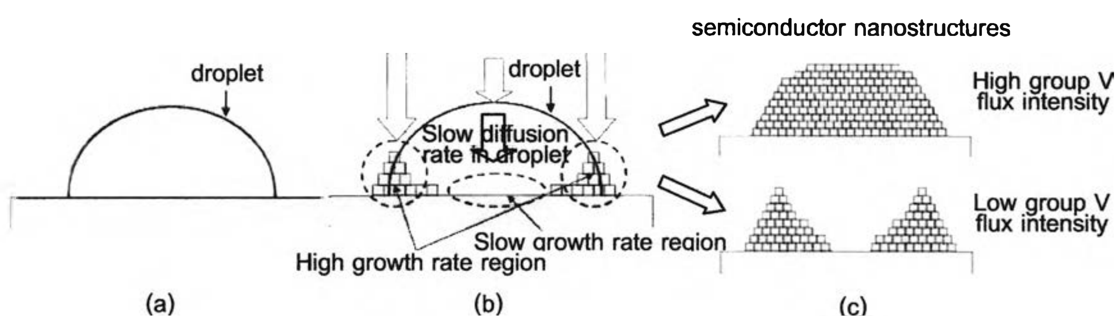

Figure 2.12 Two basic processes of droplet epitaxy technique: (a) deposition of the group III elements to crate the initial droplets (b) crystallization with the group V flux to form the semiconductor nanostructures and (c) some possible forming of semiconductor nanostructures with different group V flux intensity. (Redrawn from Mano et al., 2000)

2.3.5 Thermodynamic and Kinetic Theories of Self-Assembled Ring-Shaped Nanostructures in Non-Equilibrium System

Very recently, the droplet epitaxy has been intensively investigated as an important self-assembly technique of semiconductor QRs in the lattice-matched systems such as GaAs/AlGaAs (Mano, 2005) and the lattice-mismatched systems such as InGaAs/GaAs (Mano, 2000; Lee et al., 2009). The QRs self-assembly upon droplet epitaxy is a thermodynamic nonequilibrium process. Li and Yang (2009) have established a thermodynamic model for the nucleation of QRs and have developed a kinetic process for the growth mechanisms of the QRs self-assembly upon the droplet epitaxy as follows.

The droplet epitaxy growth is far from the thermodynamic equilibrium because the crystallization temperature of group V flux into droplets is usually not higher than 300 °C upon the droplet epitaxy. Accordingly, any thermodynamic approaches are limited seriously to describe the droplet epitaxy. The growth is mainly controlled by kinetic factors. The diffusions of atoms determine the final assembled size and shape of nanostructures. Generally, the diffusions of atoms include the diffusion of group III atoms away from liquid droplets and the trapping of group V atoms by crystallizing with them. Therefore, they play key roles in the determination of the final shape of nanostructures. The kinetic process of droplet with group V ambience is schematically illustrated in figure 2.13. The evaporation of group III from the surface is neglected because of the low vapor pressure of group III. Therefore, the loss of group III atoms only is caused by group III crystallization with group V atoms. According to the diffusion of group III atoms, the substrate surface with droplets is divided into three regions: (i) the surface of droplet (region I), (ii) the diffusion region of group III atoms (region II), and (iii) the region without diffused group III atoms (region III). Note that the diffused group III atoms away from the droplet can crystallize with group V atoms only in the two places: region II with deposited group V atoms directly from the flux and the boundary between the regions II and III with trapped group V atoms from the region III. The size of the region II, r_c, represents the diffusivity of group III atoms and the trapping ability of group V atoms.

Definitely, the balance of two different diffusion processes of group III atoms determines the final shape of nanostructures such as dot or single ring. The diffusion of group V atoms into a droplet is a significant process, and the formation of dot shape is preferable to that of ring shape in the case of high group V flux supply. However, the

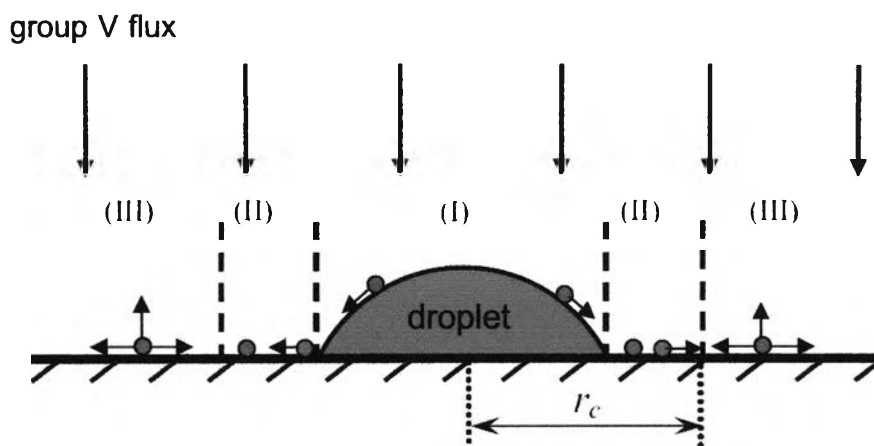

Figure 2.13 Schematic illustration of the kinetic process of group III droplet with group V ambience. The arrows denote the direction of surface diffusions of group V atoms (green points) and group III atoms (red points) (Redrawn from Li and Yang, (2009).

diffusion of group V atoms on the surface of droplet and substrate can cause the crystallization on the skirt of the droplet. When the group V flux intensity is low, the surface diffusion of group III atoms becomes more significant, and the crystallization on the skirt of the droplet results in the formation of single ring shape.

In this kinetic theory, the main study of the growth mechanisms focuses on single ring structure, which is formed in the case of the low group V flux intensity. Neglecting the diffusion of group V atoms into droplets, consequently, the crystallization of group V atoms and group III atoms only happens in following three regions: the skirt of group III droplet (the boundary between regions I and II), the diffusion region of group III atoms (region II), and the boundary between regions II and III. The action of deposited group V atoms can be divided into three conditions according to the deposited regions.

(i) When group V atoms are deposited on the surface of droplets, some deposited group V atoms diffuse on the surface of droplet and some deposited group V atoms arrive at the boundary of group III droplet and then crystallize with group III atoms.

(ii) All the deposited group V atoms in region II can be considered to crystallize with diffused group III because there are enough diffused group III atoms in the region.

(iii) When group V atoms are deposited on the surface of region III, group V atoms can rebound or diffuse randomly on the surface of substrate. The diffused group V atoms that arrive at the boundary between regions of II and III can crystallize with the

diffused group III atoms. Accordingly, there is a distinct borderline of single ring nanostructures which means that the diffused group III atoms are confined in a finite region, group III atoms cannot diffuse everywhere. Therefore, the concentration of group III atoms at the boundary of the finite region is zero because there are no group III diffused atoms at the outside of the finite region.

The kinetic diffusion is defined to be the random walk of group III atoms from the high concentration droplet to the low concentration boundary between regions II and III. According to the Fick's law, the amount of diffused group III atoms (N_{III}) in the boundary per unit time can be written as

$$N_{III} = 2\pi h_0 D_{III} C_0 \ln\left(\frac{r_{III}}{r_c}\right) \tag{2.26}$$

in which h_0 is the thickness of monolayer, C_0 refers to the concentration of group III atoms on the droplet boundary, r_{III} is atomic radius of group III atoms, r_c is the trapping radius of droplet and D_{III} represents the diffusion coefficient of group III atoms, which is given by

$$D_{III} = D_{0,III} \exp\left(-\frac{E_{III}}{kT}\right) \tag{2.27}$$

where $D_{0,III}$ is the prefactor, E_{III} is the diffusion barrier energy, and k is the Boltzmann constant, T is temperature (K). The amount of the trapped group V atoms (N_V) by diffused Group III atoms from region III per unit time can be given by

$$N_V = 2\pi r_c a_0 R\left(\frac{\nu_1}{\nu_0}\right)\exp\left(\frac{E_a - E_d}{kT}\right) \tag{2.28}$$

in which r_c is the trapping radius of droplet, a_0 is the space between surface sites, ν_1, ν_0 are the thermal vibration frequencies for the upward and lateral directions, E_a and E_d are the adsorption energy and the energy barrier for the hopping between surface sites, k is the Boltzmann constant, T is temperature (K) and R is the amount of impacting group V atoms on the substrate per unit time which can be written as

$$R = \frac{P}{\sqrt{2\pi mkT}} \tag{2.29}$$

where P is the intensity of group V flux and m is the mass of an group V atom, k is the Boltzmann constant and T is temperature (K). In order to satisfy the condition that all the migratory group III atoms from the droplet can crystallize with the trapped group V atoms and the concentration of group III atoms boundary between regions II and III is zero, the amount of the diffusing group III atoms to the boundary should be the equal of the amount of the trapped group V adatoms, $N_{III}=N_V$. Therefore, the size of region II (r_c) can be attained as follows:

$$r_c \ln\left(\frac{r_c}{r_{III}}\right) = \frac{h_0 D_{0,III} C_0 v_0}{a_0 v_1} \frac{\sqrt{2\pi mkT}\exp\left(\frac{\Delta E}{kT}\right)}{P} \tag{2.30}$$

The amounts of product of crystallization, III-V compound semiconductor, in different regions determine the final shape of nanostructures ($N_{(i)\text{III-V}}$), and the total amount per unit time ($N_{\text{III-V}}$) can be written as

$$N_{(i)\text{III-V}} = \begin{cases} \pi r_{III}^2 P / \sqrt{2\pi mkT} & (i = \text{A, at boundary of regions I and II}) \\ \pi\left(r_c^2 - r_{III}^2\right) P / \sqrt{2\pi mkT}\, DC & (i = \text{B, in regions II}) \\ 2\pi h_0 D_{III} C_0 \ln\left(\frac{r_{III}}{r_c}\right) & (i = \text{C, at boundary of regions II and III}) \end{cases} \tag{2.31}$$

$$N_{III\text{-}V} = N_{(A)\,III\text{-}V} + N_{(B)\,III\text{-}V} + N_{(C)\,III\text{-}V} \tag{2.32}$$

Considering the equal between the consumed amount of group III atoms and the produced III-V compound semiconductor during the crystallization process, the change in volume of droplet (V_{droplet}) in a short time (Δt) can be given by

$$V_{droplet}(t + \Delta t) = V_{droplet}(t) - N_{III-V} V_{m,III} \frac{\Delta t}{N_A} \tag{2.33}$$

where $V_{m,III}$ is the molar volume of droplet and N_A is the Avogadro constant. The corresponding radius of droplet during the crystallization process can be calculated by the geometrical relation. Making clear the amounts of the produced III-V compound semiconductor in different regions and change in size of droplet during the crystallization process, the shape evolution of nanostructure can be deduced from equations (2.30) and (2.31). The change in height of nanostructure (Δh) at the point of r (the distance from the center of droplet) in a limit time Δt and the final height (h) at the point of r in the total time of crystallization process t_m can be calculated as follows:

$$\Delta h(r,t) = \begin{cases} \dfrac{N_{(A)III-V} V_{m,III-V} \Delta t}{N_A \pi \left[r_c^2(r) - r_c^2(r+\Delta t)\right]} & [r_c(t+\Delta t) < r < r_c(t)] \\ \dfrac{N_{(B)III-V} V_{m,III-V} \Delta t}{N_A \pi \left[r_c^2(r) - r_{III}^2(t)\right]} & [r_{III}(t) < r < r_c(t+\Delta t)] \\ \dfrac{N_{(C)III-V} V_{mIII-V} \Delta t}{N_A \pi \left[r_{III}^2(r) - r_{III}^2(r+\Delta t)\right]} & [r_{III}(t+\Delta t) < r < r_{III}(t)] \end{cases} \quad (2.34)$$

$$\Delta h(r,t) = \sum_{t=0}^{t_m} \Delta h(r,t) \quad (2.35)$$

In this model, we do not consider the substrate orientation. Thus the diffusions of group III atoms on the substrate surface in all directions are equivalent. The surface distance between the calculated point and the boundary of droplet is only considered in the horizontal distance. However, it can reveal the simple nonequlibrium kinetic process of droplet epitaxy technique for more understanding.

2.4 Quantum Information Processing

In the early 1990s Lent et al. (1993) demonstrated a quantum information processing configuration of a pair of tunneled electrons contained in a quantum-dot cell that calls a quantum-dot cellular automata (QCA) cell. In the classical QCA cell, the electrons owing to electrostatic repulsion align along one of the two diagonal configurations that correspond to their maximal spatial separation. The QCA cell thus has the ability to encode two states – two logic values (0 and 1). Moreover, Bajec et al.

(2006) also introduced the extended QCA (EQCA) cell by extending the QCA cell with four additional quantum dots. The classical QCA cell is extended in the sense of an enlarged range of its possible stable and usable states. The semi-classical modeling approach showed that the range of possible states can be increased from two to three, giving the EQCA cell the ability to encode the logic values (0, 1/2 and 1) by using a special interpretation of electron configurations in the EQCA. This primary motive is to promote the idea of finally switching focus from pure miniaturization and the top-down concept to the bottom-up concept and start extending the currently available approaches to allow for 'richer' processing and data storage capabilities without a major increase in space requirements. Therefore it is a motivation of this work to fabricate the ring-shaped QDMs for this application.

2.4.1 Quantum Cellular Automata

One nanostructure paradigm, proposed by Lent et al. (1993), is Quantum-dot cellular automata (QCA), which employs arrays of coupled quantum dots to implement Boolean logic functions. The advantage of QCA lies in the extremely high packing densities possible due to the small size of the dots, the simplified interconnection, and the extremely low power-delay product. A basic QCA cell consists of four quantum dots in a square array coupled by tunnel barriers. Electrons are able to tunnel between the dots, but cannot leave the cell. If two excess electrons are placed in the cell, Coulomb repulsion will force the electrons to dots on opposite corners. There are thus two energetically equivalent ground state polarizations, as shown in figure 2.14, which can be labeled logic "0" and "1". Coulombic interactions between the electrons cause the cell to exhibit highly bistable switching between these two polarizations. Since the cells are capacitively coupled to their neighbors, the ground state of the line is for all cells to have the same polarization. When several cells are lined up to form a wire and a given logic value enforced to the input cell, it will propagate along the wire in a domino fashion until all cells have reached the same configuration as show in figure 2.15. Since the former means that the logic value 0 or 1 enforced (input) on one end of the wire is propagated to its other end (output), the wire is called *a binary wire*. The mapping of a combinational logic

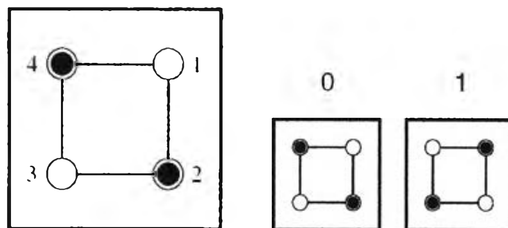

Figure 2.14 Layout of the four-dot QCA cell with two electrons and the two distinct electron configurations corresponding to their maximum spatial separation, which can be labeled logic “0” and “1”.

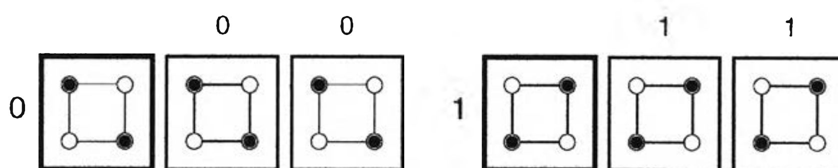

Figure 2.15 The binary wire; propagation of enforced logical values 0 and 1 along a line of QCA cells.

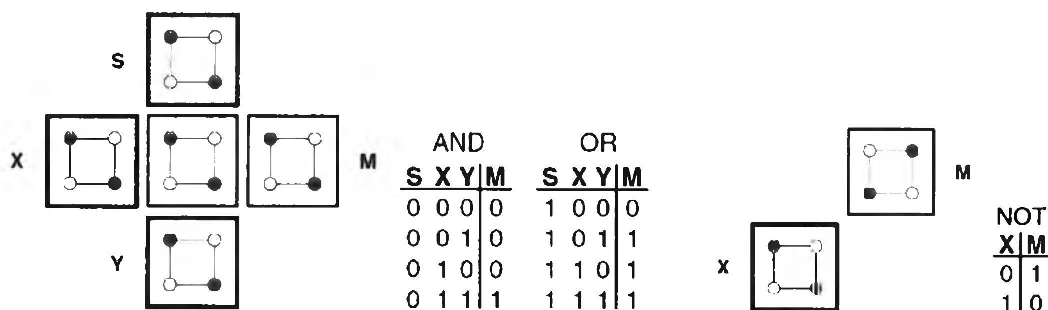

Figure 2.16 The QCA majority gate: AND, OR, and NOT.

problem onto a QCA system can be accomplished by finding arrangements of QCA cells that implement the basic logic functions AND, OR, and NOT as shown in figure 2.16. Memory can also be implemented using QCA cells, making general purpose computing possible. The ability to transfer data and the functionally complete set of logic functions enables the construction of any given switching structure.

2.4.1 Extended Quantum Cellular Automata

The EQCA cell is an eight-dot QCA cell with the structure presented in figure 2.16. The dots are evenly distributed in a circular fashion, and again separated by tunneling barriers. Due to the electrostatic repulsion similar to the QCA cell, the electrons in EQCA cell tend to align along one of the configurations that correspond to their maximal spatial separation. There are four distinct configurations with maximal spatial separation between electrons. For the diagonal configurations, the same association as in the classical QCA case is used. The configuration with electrons in dots 2 and 4 is thus associated with the logic value 0 and the configuration with electrons in dots 1 and 3 with the logic value 1. The vertical configuration (i.e. electrons in dots 5 and 7) and the horizontal configuration (i.e. electrons in dots 6 and 8) are denoted as configurations 'A' and 'B' as presented in figure 2.17.

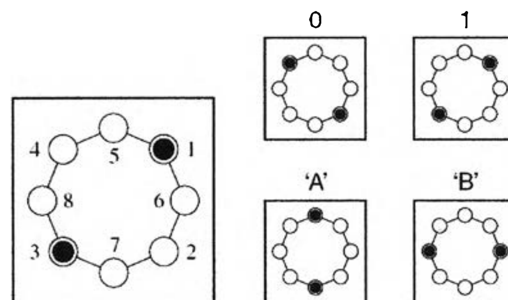

Figure 2.17 Layout of the eight-dot EQCA cell with two electrons and the four distinct electron configurations corresponding to their maximum spatial separation, which can be labeled logic "0", "1" and "1/2".

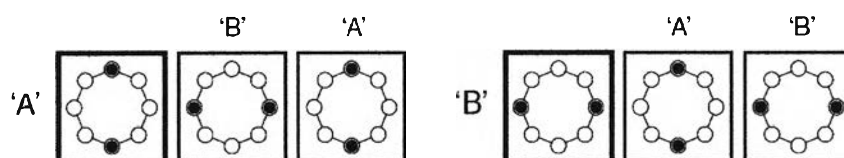

Figure 2.18 The ternary wire; propagation of enforced configuration 'A' or 'B' along a line of EQCA cells.

AND				OR			
S	X	Y	M	S	X	Y	M
0	0	0	0	1	0	0	0
0	0	½	0	1	0	½	½
0	0	1	0	1	0	1	'B'
0	½	0	0	1	½	0	½
0	½	½	½	1	½	½	½
0	½	1	½	1	½	1	1
0	1	0	'B'	1	1	0	1
0	1	½	½	1	1	½	1
0	1	1	1	1	1	1	1

Figure 2.19 The EQCA majority gate truth table, AND and OR.

Like in the case of the binary wire, when several cells are lined up to form a wire and either the logic value 0 or 1 is enforced to the driver cell, it will propagate along the wire, until all cells have reached the same configuration. Modeling in figure 2.18 showed that 'A' or 'B' will propagate along the wire in an alternating fashion, such as for example ABABABAB. . .. By associating both configurations 'A' and 'B' with the logic value ½, the functionality of the wire gets extended making it capable of propagating three logic values 0, ½ and 1 making it *a ternary wire*. Figure 2.19 shows the EQCA majority gate truth table, AND and OR. In a functionally set of logic functions EQCA cell study still has some problems. For the inverter or NOT, worked perfectly, giving the correct output for any given input. When the input logic values is 0 and 1, it behaved just as the QCA inverter and if the configuration enforced either 'A' or 'B', the configuration of the target cell did not change at all. But in the case of AND(1,0) and OR(0,1) processing, they have the problems in both by reaching configuration 'B' instead of returning 0 and 1, respectively. Although, this sole objective still under progress to translate configuration 'B' into the correct output value, this application wise is a motivation of this work to fabricate the ring-shaped QDMs.

2.5 Material Considerations

The self-assembled growth, which can be used to realize QD structures, can be done in several semiconductor material systems such as In(Ga)As/GaAs, InP/InGaP, and SiGe/Si, because the preliminary condition for the growth is only that the QD material have a larger lattice constant and a smaller band gap compared with substrate material.

Figure 2.20 shows the relationship between band gap energy and the lattice constant of III-V material systems. This work concentrates only on the InP/$In_{0.5}Ga_{0.5}P$/GaAs material system.

Phosphorus containing semiconductors have obtained a great import in the world of ultra-high speed devices and circuits. Since the early of 1990s, the studies of InP QDs are based gas-sources such gas-source MBE (GS-MBE) and metalorganic chemical vapour deposition (MOCVD). There are a few reports about solid-sources MBE (SS-MBE) growth of InP QDs due to the problem on the vapor pressure control of phosphorus and several problems in including phosphides in the conventional MBE growth process. A major concern is the occurrence of phosphorous tetramers (P_4) which has a lower sticking coefficient and condenses as white phosphorus having high vapor pressure, inflammability and toxicity. These properties require additional technical measures in

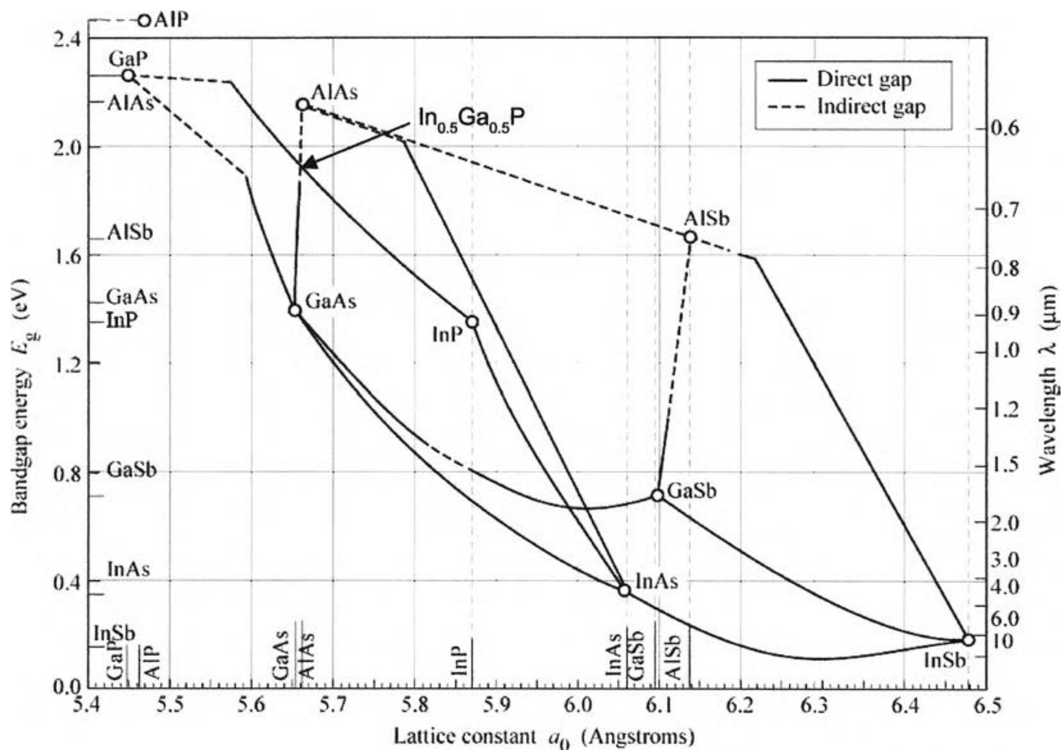

Figure 2.20 Lattice constant versus energy gap at room temperature for the III-Vs material system. The solid line is for direct band gap material and the dotted line is for indirect band gap material.

I 87564708

order to grow phosphorus in the vacuum environment of MBE system. Thus, in recent years, growth of techniques using phosphine (PH_3) has become standard for the fabrication of phosphides. However, PH_3 is not ideal either, because it is highly toxic and often introduces water vapor contamination. Therefore, investigations into alternative sources, either a less toxic liquid source cell such as teriary-butyl-phosphine or solid-source, are required. There are two methods have been obtained to generate for solid-source phosphorus. One is value-cracker effusion cell. The other is sublimation of phosphorus from phosphines such as InP and GaP. Initially the sublimation cell was considered to unsuitable for epitaxial growth of ternary and quaternary compounds because it produced not only P_2 but also some amount of group III material. After improving, the pure phosphorous dimers (P_2) molecular beam can be generated from a decomposition source with a scavenger which traps the parasitic group III flux. This cell has only a very small amount of white phosphorus accumulates in the chamber, therefore, GaP decomposition source is used in this work as the P_2 source in SS-MBE system. This system has many advantages such as high operating temperature (≈900–1000°C), very stable and reproducible BEP, high P_2/P_4 ratio (≈150), very low parasitic Ga BEP ($Ga:P<10^{-3}$) (Jin-Phillipp and Phillipp, 2000). Properties of InP, $In_{0.5}Ga_{0.5}P$ and GaAs semiconductors at room temperature that consider in this work are present in table 2.1. All of InP, $In_{0.5}Ga_{0.5}P$ and GaAs semiconductors are zinc blende crystal structure as shown in figure 2.21. From equation (2.11), the lattice mismatch between InP and $In_{0.5}Ga_{0.5}P$ is 3.8 % while $In_{0.5}Ga_{0.5}P$ has lattice match with GaAs substrate.

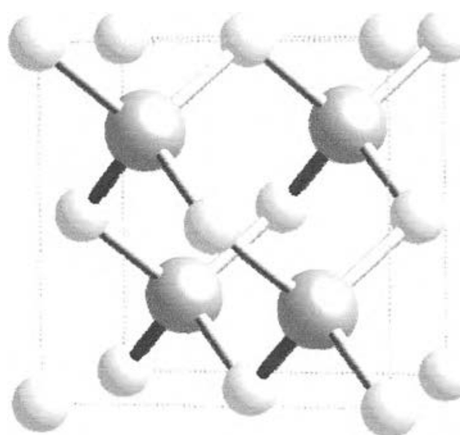

Figure 2.21 The zinc blende crystal structure.

Table 2.1 Properties of InP, $In_{0.5}Ga_{0.5}P$ and GaAs semiconductors at room temperature (300 K) (Jalali and Pearton, 1995).

Parameter	InP	$In_{0.5}Ga_{0.5}P$	GaAs
Crystal structure	Zinc blende	Zinc blende	Zinc blende
Band gap type	direct	direct	direct
Energy gap, E_g (eV)	1.344	1.92	1.424
Lattice constant (Å)	5.8687	5.653	5.65325
Number of atoms (cm^{-3})	$3.96 \cdot 10^{22}$	$4.46 \cdot 10^{22}$	$4.42 \cdot 10^{22}$
Melting point (°C)	1062	1265	1240
Effective electron mass, m_e	$0.08m_0$	$0.088m_0$	$0.063m_0$
Effective hole masses, m_h	$0.6m_0$	$0.7m_0$	$0.51m_0$
Elastic constant, C_{11} ($\times 10^{11}$ dyn/cm^2)	10.11	12.0406	11.879
Elastic constant, C_{12} ($\times 10^{11}$ dyn/cm^2)	5.61	5.8991	5.376
[100] Poisson ratio, υ_{PR}	0.36	0.3355	0.31
[100] Young's modulus ($\times 10^{11}$ dyn/cm^2)	6.11	8.1631	8.59